International Journal of Heat and Fluid Flow 30 (2009) 1067–1079

Contents lists available at ScienceDirect

International Journal of Heat and Fluid Flow

journal homepage: www.elsevier.com/locate/ijhff

Large-eddy simulations of chevron jet flows with noise predictions

Hao Xia, Paul G. Tucker *, Simon Eastwood

Whittle Laboratory, Department of Engineering, University of Cambridge, Cambridge, CB3 0DY, UK

ARTICLE INFO

Article history:
Received 12 December 2008
Received in revised form 16 March 2009
Accepted 22 May 2009
Available online 24 June 2009

Keywords:
Reynolds-averaged Navier–Stokes equations
Implicit large-eddy simulation
Jet noise
Chevron nozzle
Ffowcs Williams–Hawkings integral

ABSTRACT

Hybrid large-eddy type simulations for chevron nozzle jet flows are performed at Mach 0.9 and $Re = 1.03 \times 10^6$. Without using any subgrid scale model (SGS), the numerical approach applied in the present study is essentially implicit large-eddy simulation (ILES). However, a Reynolds-averaged Navier–Stokes (RANS) solution is patched into the near wall region. This makes the overall solution strategy hybrid RANS–ILES. The disparate turbulence length scales, implied by these different modeling approaches, are matched using a Hamilton–Jacobi equation. The complex geometry features of the chevron nozzles are fully meshed. With numerical fidelity in mind, high quality, hexahedral multi-block meshes of 12.5×10^6 cells are used. Despite the modest meshes, the novel RANS–ILES approach shows encouraging performance. Computed mean and second-order fluctuating quantities of the turbulent near field compare favorably with measurements. The radiated far-field sound is predicted using the Ffowcs Williams and Hawkings (FW–H) surface integral method. Encouraging agreement of the predicted far-field sound directivity and spectra with measurements is obtained.

1. Introduction

Noise during airplane take-off is one of the key issues concerning both airframe and aero-engine manufactures. This is a direct consequence of today's rapidly increasing demand for civil air transport. As many new policies and measures have been set out to tackle environmental noise, the drive for aircraft and aero-engine manufactures to develop new conceptual nozzles for quieter engines are emerging. One of the current main conceptual noise reduction ideas is the chevron nozzle concept (Bridges and Brown, 2004), shown in Fig. 1. The potential for chevron nozzles to provide noise reductions is significant. Measurements have suggested that certain chevron nozzles can provide nearly 3 dB of noise reduction during take-off with less than 0.5% thrust loss during cruise (Saiyed, 1997, 2000). Chevrons typically reduce the low-frequency noise observed downstream (at low polar angles) while increasing the high-frequency perceived by an observer orthogonal to the jet axis (polar angle ~90°). The stream-wise vortices generated by the chevrons enhance the shear layer mixing. This leads to changes in noise level over certain frequency ranges. The ultimate goal in chevron design is to decrease the low-frequency noise as much as possible while preventing a significant increase in high-frequency noise. Parameters which can be varied for this problem are the chevron count, penetration (or bend angle) and length. Chevron count controls the spacing between the axial vortices generated by the chevrons. Penetration controls the strength of the axial vorticity. Length controls the distribution of vorticity within the axial vortices (Bridges and Brown, 2004).

Chevron RANS solutions have been performed by Kenzakowski et al. (2000, 2005), Thomas et al. (2001), Engblom et al. (2004), and Massey et al. (2006). Birch et al. (2006) concluded that the calibrated RANS based noise prediction procedure employed by these workers could not fully account for the effect of chevrons on the complex flow physics. On the other hand, LES has shown promise despite many open questions and difficulties (Bodony and Lele, 2008). Several chevron studies (Shur et al., 2005, 2006; Uzun and Hussaini, 2007; Xia et al., 2008) have demonstrated the potential of LES for studying the complex flow physics in the downstream near-nozzle region. Shur et al. (2005, 2006) made the first successful LES noise prediction for chevron jets. Notably explicit resolution of the chevron geometry was avoided. Instead an emulation procedure to mimic the effect of real chevrons is used. Uzun and Hussaini (2007) studied the near-nozzle region of the Bridges and Brown (2004) SMC001 (5° bend) nozzle using ILES type simulations. A prefactored fourth-order compact scheme with a sixth-order spatial filter and overlapped meshes with up to 100 million nodes were used. Their goal was to somehow explore the capability of LES when resolving high-frequency noise sources. In the study of Xia et al. (2008), the exact SMC001 and SMC006 (18.2° bend) chevron geometries were meshed with body-fitted grids. A hybrid RANS–ILES numerical method was adopted comprising near wall RANS and implicit LES (or ILES) away from walls. Despite the modest (largest) 12.5 million-node grid, the preliminary results for both near field turbulent statistics and far-field sound showed encouraging agreement with measurements.

* Corresponding author. Tel.: +44 1223 337582; fax: +44 1223 337596.
E-mail addresses: hx222@cam.ac.uk (H. Xia), pgt23@cam.ac.uk (P.G. Tucker), se282@cam.ac.uk (S. Eastwood).

0142-727X/$ - see front matter © 2009 Elsevier Inc. All rights reserved.
doi:10.1016/j.ijheatfluidflow.2009.05.002

Nomenclature

a	speed of sound
$\mathbf{A}$	Jacobian, $\mathbf{A} = \partial\mathbf{F}/\partial\mathbf{Q}$
D	jet diameter at the nozzle exit
d	standard wall distance
d_c	RANS cut-off wall distance
d	modified wall distance
$d\mathbf{r}$	displacement vector
δ_{ij}	Kronecer delta
δ_m	shear layer momentum thickness
Δ	grid spacing
ε	upwinding control parameter
$\varepsilon_0, \varepsilon_1$	Hamilton–Jacobi blending function control parameters
e	internal energy
E	total energy
f, g	Hamilton–Jacobi blending functions
$\mathbf{F}$	flux vector
$\mathbf{F}^{inv}$	inviscid flux vector
$\mathbf{F}^{vis}$	viscous flux vector
Ma	Mach number
n_j	outward unit normal vector component
$\mathbf{Q}$	vector of primitive variables, $(\rho, \rho u_i, E)^T$
p	static pressure of the fluid
p'	pressure fluctuation
p'_{rms}	root-mean-square pressure fluctuation
R	gas constant; far-field sound measurement distance
Re	Reynolds number
ρ	density
S	FW–H surface; Nominal sound source
S_{ij}	strain rate tensor
t	dimensional time
t^*	non-dimensional time tU_j/D
Δt	time step
τ_{ij}	stress tensor
θ	circumferential direction
Θ	far-field sound measuring angle
U	time-average of velocity u
u, v, w	velocity components in x, y, z direction, also used in u_1, u_2, u_3 form
u_n	normal velocity
u'	fluctuation of u, i.e. $u' = u - U$
u_r	radial velocity component
u_θ	circumferential velocity component
μ, μ_T	molecular viscosity, eddy viscosity
$\boldsymbol{\omega}$	vorticity vector
ω_x	x-vorticity (stream-wise vorticity)
X, Y, Z	normalized x, y, z by D
x, y, z	Cartesian Coordinates, also as x_1, x_2, x_3
$y+$	non-dimensional wall distance

Subscripts

0	total condition
ac	acoustic condition
c	cell center
j	jet exit condition
L/R	immediate left/right of the common face
n	outward normal direction
T	turbulent value
∞	ambient condition

Other Symbols

$\bar{(\,)}$	time-averaged/mean quantity
$\tilde{(\,)}$	Favre-filtered quantity; modified quantity

Subgrid scale (SGS) stress modeling divides the LES community with, for example, constant coefficient or dynamic coefficient SGS, non-linear models (Liu et al., 2008) or using no model, but in conjunction with the numerical dissipation (and other traits) of the scheme (often loosely referred to as ILES) taking place. The attractions of ILES have been discussed widely. Grinstein and Fureby (2002) showed that ILES can capture well some complex jet noise vortex dynamics. Shur et al. (2003) successfully used ILES, or "Coarse-grid DNS" in their terms, for jet noise predictions. Bogey and Bailly (2005) noted that the effects of using a subgrid scale model are not well understood with for example SGS eddy viscosity corrupting some high-frequency noise components. The above cited chevron LES studies are all essentially implicit LES but show promising results. It is worth noting, as demonstrated by Ghosal (2002), and Chow and Moin (2003), that disentangling numerical influences from those of the SGS model is a daunting task that dilutes the SGS model's value. The numerical dissipation when combined with that of the SGS model can result in an excess of dissipation (Tucker, 2006). However, when an adverse pressure gradient is present in a boundary layer, a laminar type boundary velocity profile is prone to separate non-physically, dramatically altering the subsequent downstream flow development. Therefore,

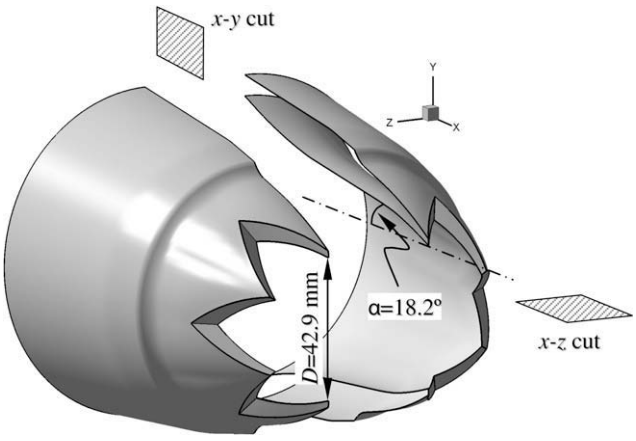

Fig. 1. Sectioned view of the chevron nozzle studied by Bridges and Brown (2004).

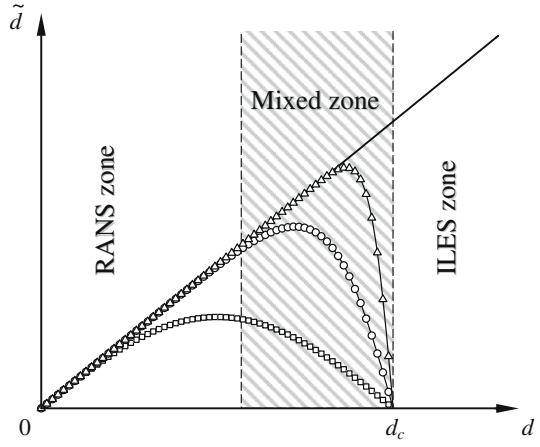

Fig. 2. Hybrid RANS–ILES turbulence length/distance scales: —, non-modified scale; —□—, $\varepsilon_0 = 0.2$, $\varepsilon_1 = 0$; —○—, $\varepsilon_0 = 0.2$, $\varepsilon_1 = 2$; —△—, $\varepsilon_0 = 0.1$, $\varepsilon_1 = 1$.

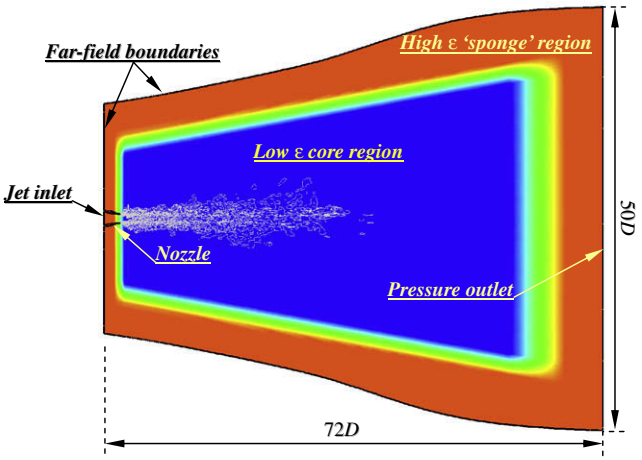

Fig. 3. Definition of domain, boundaries and 'sponge' zone.

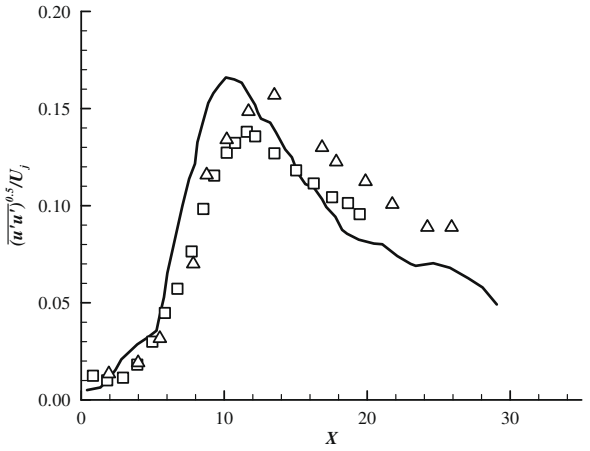

Fig. 4. Normal centre line Reynolds stress $\overline{u'u'}$.—, Prediction. Measurements (Bridges and Wernet, 2003):□, LDV; △, PIV.

if it cannot be fully resolved, the boundary layer needs some empirical treatment. A hybrid RANS–ILES approach was proposed by Tucker (2002, 2004) with a Hamilton–Jacobi equation blending the RANS and ILES zones. This has been further applied to chevron jets by Xia et al. (2008).

As a follow-up of our previous work, detailed results of both SMC001 and SMC006 nozzles are presented in this paper with more focus on the SMC006 nozzle. The hybrid RANS–ILES methodology remains the key numerical feature, but this time with Spalart–Allmaras (1992) near wall RANS modeling. This paper is organized as follows. First, the numerical methods section gives a brief description of the governing equations, discretization schemes, boundary conditions, the FW–H acoustic post-processor and validation. Then the simulation setup and flow conditions are briefly given. In the results section, the instantaneous and time averaged velocity, vorticity and turbulent statistics fields are presented. Finally the far-field noise for both nozzles will be discussed, based on the calculated far-field sound pressure level directivity and the power spectral density.

2. Numerical methods

2.1. Governing equations

The Favre-average/filtered compressible Navier–Stokes equations for ideal gas are solved. The conservative form of the continuity, momentum and energy equations can be expressed as

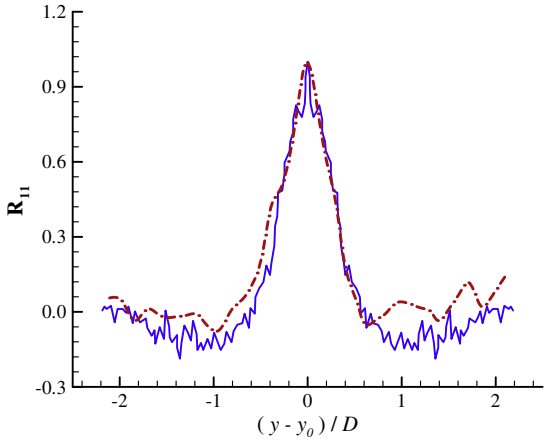

Fig. 5. Two-point spacial correlation $\mathscr{R}_{11}$ at $x_0 = 16D$, $y_0 = 0$. -·-·-, Prediction. —, Measurement (Bridges and Wernet, 2003).

$$\frac{\partial \bar{\mathbf{Q}}}{\partial t} + \frac{\partial \bar{\mathbf{F}}_i^{inv}}{\partial x_i} - \frac{\partial \bar{\mathbf{F}}_i^{vis}}{\partial x_i} = 0 \tag{1}$$

The conservative variables are defined as $\bar{\mathbf{Q}} = [\bar{\rho}, \bar{\rho}\tilde{u}_i, \tilde{E}]^T$. The inviscid and viscous fluxes are respectively given by $\bar{\mathbf{F}}_i^{inv} = \tilde{u}_i\bar{\mathbf{Q}} + [0, \delta_{1i}\bar{p}, \delta_{2i}\bar{p}, \delta_{3i}\bar{p}, \bar{p}\tilde{u}_i]^T$ and $\bar{\mathbf{F}}_i^{vis} = [0, \tilde{\tau}_{1i}, \tilde{\tau}_{2i}, \tilde{\tau}_{3i}, \tilde{\tau}_{ki}\tilde{u}_k + \tilde{q}_i]^T$, with the stress tensor $\tilde{\tau}_{ij}$, total energy $\tilde{E}$ and heat flux $\tilde{q}_j$ being formulated as

$$\tilde{\tau}_{ij} = 2(\mu + \mu_T)\left(\tilde{S}_{ij} - \frac{1}{3}\frac{\partial \tilde{u}_j}{\partial x_j}\delta_{ij}\right), \quad \tilde{E} = \bar{\rho}\tilde{e} + \frac{1}{2}\bar{\rho}\tilde{u}_i\tilde{u}_i, \quad \tilde{q}_i = -(k + k_T)\frac{\partial \tilde{T}}{\partial x_i} \tag{2}$$

The state equation $\bar{p} = \bar{\rho}R\tilde{T}$ defines the relation between pressure, density and temperature for ideal gas.

For the RANS part, the Spalart–Allmaras model is used. The modeled eddy viscosity, μ_T, is defined by

$$\mu_T = \bar{\rho}\frac{\tilde{\nu}}{f_{v1}} \tag{3}$$

where the modified kinematic eddy viscosity, $\tilde{\nu}$, satisfies the following transport equation,

$$\frac{D\tilde{\nu}}{Dt} = c_{b1}\tilde{S}\tilde{\nu} - c_{w1}f_w\left(\frac{\tilde{\nu}}{d}\right)^2 + \frac{1}{\sigma}\left[\nabla\cdot((\nu + \tilde{\nu})\nabla\tilde{\nu}) + c_{b2}(\nabla\tilde{\nu})^2\right] \tag{4}$$

In the above $D/Dt = \partial/\partial t + \tilde{u}_i\partial/\partial x_i$ is the material derivative. Closure coefficients and functions follow the original definition of Spalart and Allmaras (1992).

2.2. Hybrid RANS–ILES

The RANS and ILES regions can also be defined via the nearest wall distance d and also, if desired, blended through its modification to $\tilde{d}$. In this study, differential equation based methods are employed to calculate $\tilde{d}$. The exact d can be computed via solution of the Eikonal equation (Sethian, 1999)

$$|\nabla d| = 1 \tag{5}$$

A modified wall distance $\tilde{d}$ can be evaluated from a Hamilton–Jacobi equation (Tucker, 2004),

$$|\nabla\tilde{d}| = 1 + f(\tilde{d})\nabla^2\tilde{d} + g(\tilde{d}) \tag{6}$$

and

$$f(\tilde{d}) = \varepsilon_0\tilde{d} \text{ and } g(\tilde{d}) = \varepsilon_1\left(\frac{\tilde{d}}{d_c}\right)^2$$

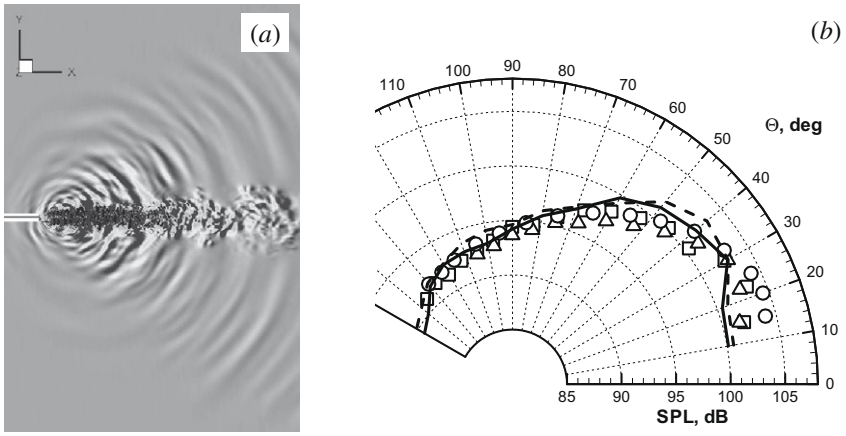

Fig. 6. Acoustic wave dilatation visualized by $\partial p/\partial t$ contours (a); and (b) SPL directivities at $R = 120D$; —, Fine mesh; - - -, Coarse mesh; □, Measurements of Lush (1971) $Re = 6 \times 10^5$; △, Measurements of Tanna (1977); ○, Measurements of Brown and Bridges (2006) $Re = 10^6$.

Table 1
Parameters of chevron nozzles computed.

Nozzle ID	Chevron no.	Bend angle (°)	Tip-to-tip distance (m)	Penetration (m)
SMC001	6	5	50.8×10^{-3}	0.985×10^{-3}
SMC006	6	18.2	42.9×10^{-3}	3.525×10^{-3}

Table 2
Jet flow conditions.

Type	p_0 (Pa)	T_0 (K)	p_∞ (Pa)	T_∞ (K)
Isothermal	1.78×10^5	286.4	0.97×10^5	280.2

where d_c is the RANS cut-off distance. Detailed discussion of the control functions f and g can be found in Tucker (2004). Sufficient to say here, it is desirable to have a smooth transition zone of the eddy viscosity field between the RANS and ILES zones, especially to help maintain good numerical stability. As shown in Fig. 2, different blending of $\tilde{d}$ at the RANS–ILES interface can be obtained by specifying different values of ε_0 and ε_1. For the chevron simulations $\varepsilon_0 = 0.1$, $\varepsilon_1 = 1$ and d_c is 60 in wall unit.

2.3. Spatial and temporal discretization

The flow solver, FLUXp, is based on a cell centered finite volume discretisation for arbitrarily unstructured meshes. More details of the solver can be found in Xia (2005). Despite the fact that high-order compact schemes (with spectral-like resolution) are preferred to minimize dispersive and dissipative numerical errors, several studies including Wu et al. (1999) and Mary and Sagaut (2002) suggest that with sufficient mesh resolution DNS and LES can be carried out with second-order schemes. Moreover, due to their efficiency and flexibility in handling complex geometry, second-order schemes have good applicability for industrial applications. Indeed, as demonstrated by Chung and Tucker (2003) compact schemes can give poor performance on highly stretched grids. Hence, second-order spatial schemes with dissipation reduction techniques are employed in this study.

To compute the inviscid flux, Roe's flux difference splitting approximate Riemann solver (Roe, 1981) is employed at the common face to two neighboring cells:

$$\mathbf{F} = \frac{1}{2}(\mathbf{F}_L + \mathbf{F}_R) - \varepsilon\frac{1}{2}|\mathbf{A}|(\mathbf{Q}_R - \mathbf{Q}_L) \tag{7}$$

In the above $|\mathbf{A}| = \mathbf{M}|\mathbf{\Lambda}|\mathbf{M}^{-1}$ is the diagonalizing transform and $\mathbf{A} = \partial\mathbf{F}/\partial\mathbf{Q}$ the Jacobian. Here, following Bui (1999), $0 < \varepsilon < 1$ is adopted as an additional parameter to control the amount of upwinding. A similar technique has also been applied by Shur et al. (2003), where it was cast in a form of blending a purely centered and a fully upwinded flux. Fig. 3 gives a typical distribution of ε. In our study its minimal value is set to 0.1 and to avoid numerical instability a continuous variation of ε is applied. A linear transition zone is indicated in Fig. 3 as the green[1] area between the blue and red regions of the lowest and highest ε values. A second-order MUSCL type reconstruction by van Leer (1979) calculates the immediate left and right values of $\mathbf{Q}$ at the cell interface from its two neighboring cell centers:

$$\mathbf{Q}_{L/R} = \mathbf{Q}_C + \nabla\mathbf{Q} \cdot d\mathbf{r} \tag{8}$$

In the above $\nabla\mathbf{Q}$ is the gradient, $d\mathbf{r}$ the displacement vector from the left or right cell center to the face center. With the absence of shock waves, the limiter is not included in Eq. (8). The viscous flux is discretized by a standard second-order centered scheme.

The dual-time integral is employed with the outer physical time discretized by a three-level backward Euler scheme. This leads to second-order temporal accuracy. The inner pseudo time is advanced by a three-stage Runge–Kutta scheme. As the outer time is discretized implicitly, larger physical time steps are allowed thus increasing the efficiency compared with explicit time marching.

2.4. Boundary conditions

As shown in Fig. 3 the computational domain consists of the upstream, jet inlet, cylindrical, and downstream boundaries. The domain is $72D$ long and expanded to a radial extent of $50D$ at the right end. On the nozzle solid wall, the no slip, impermeability velocity and adiabatic thermal conditions are applied. Nonlinear characteristic boundary conditions (Colonius, 2004) are used. In particular, Thompson's (1987) characteristic relation is applied to the far-field boundaries (upstream and cylindrical). A Rudy and Strikwerda (1980) type formulation is adopted for the outlet and jet inlet boundaries. The 'sponge' zone (area of high numerical damping) is also deployed to further damp the acoustic reflections. Moreover, avoiding spurious waves, no forcing is specified at the jet inlet.

[1] For interpretation of color in Figs. 3 and 9, the reader is referred to the web version of this article.

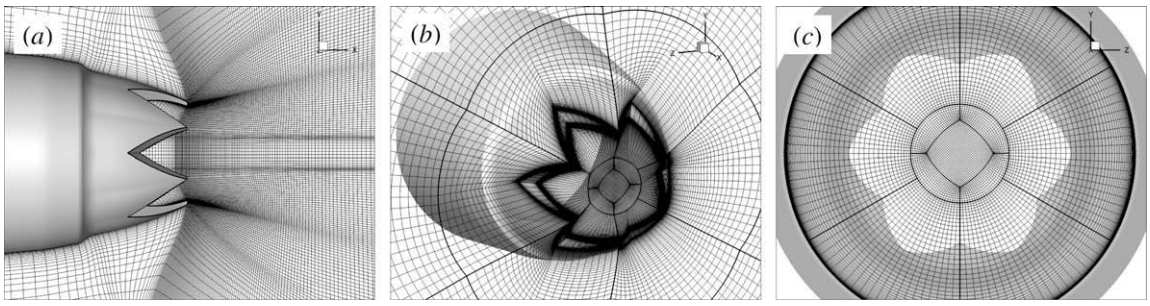

Fig. 7. SMC006 mesh on: (a) x–y cut plane (shown with half of the actual node density); (b) x-plane through the chevron edge; (c) jet inlet plane.

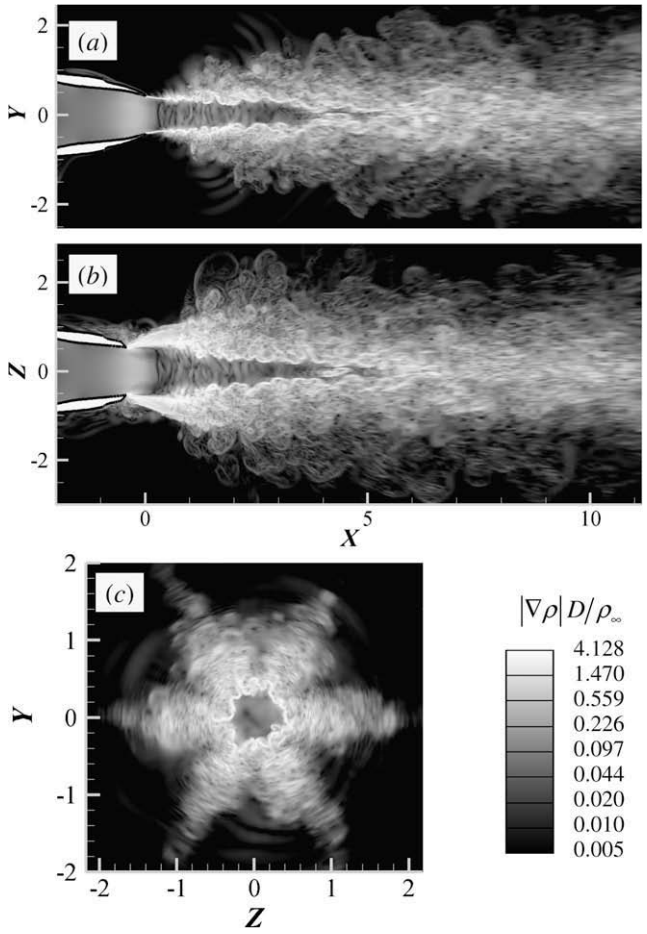

Fig. 8. Non-dimensional density gradient magnitude $|\nabla\rho|D/\rho_\infty$ or 'Numerical Schlieren' snapshots of SMC006 on cut planes: (a) x–y plane at $z = 0$; (b) x–z plane at $y = 0$; (c) z–y plane at $x = 1.5D$.

2.5. Acoustic post-processor

The surface integral, based on the Ffowcs Williams–Hawkings (1969) equation, is computed. This yields the far-field acoustic pressure fluctuation $p'(\mathbf{x}, t)$. Since the noise source is inside the surface (if the surface is large enough and far enough from the jet exit region), a simplification can be made by omitting the volume quadrupole integral. This, as suggested by Shur et al. (2003) and Tucker (2004), saves substantial data storage. The integral equation is as follows:

$$4\pi|\mathbf{x}|p'(\mathbf{x},t) = \frac{x_j}{|\mathbf{x}|a_\infty}\frac{\partial}{\partial t}\left[\int_S (p'n_j + \rho u_j u_n)dS\right] + \frac{\partial}{\partial t}\left[\int_S \rho u_n dS\right] \quad (9)$$

In the above, $\mathbf{x}$ defines the observer position, a_∞ stands for the ambient speed of sound and S is the FW–H surface. The quantities in the square brackets are computed at "retarded" times. Also, n_j is the component of the unit outward normal vector on the surface, and u_j is the velocity component. Surface data is stored while the simulation is performed ready for later post-processing. This gives flexibility, avoiding re-running the whole simulation if anything needs to be changed in the post-processing process.

2.6. Validations for a Ma = 0.9 basic round jet

To test the eddy resolving capabilities of the numerical solver, extensive studies of Tucker et al. (2006) for the basic round jet flow on meshes with various node densities have been performed. It is perhaps worth presenting some typical results here again to give some background to the solver performance. This benchmark unheated case has a $Ma = 0.9$ and $Re = 1 \times 10^4$ (as usual based on the jet diameter and the jet velocity U_j). Half and five million-cell meshes similar in topology to the one in Shur et al. (2003) are used.

Fig. 4 compares the predicted and measured (Bridges and Wernet, 2003) centerline peak normal stress. The measurements are given by symbols and the line gives the prediction. As can be seen the agreement is encouraging. Fig. 5 plots two-point velocity

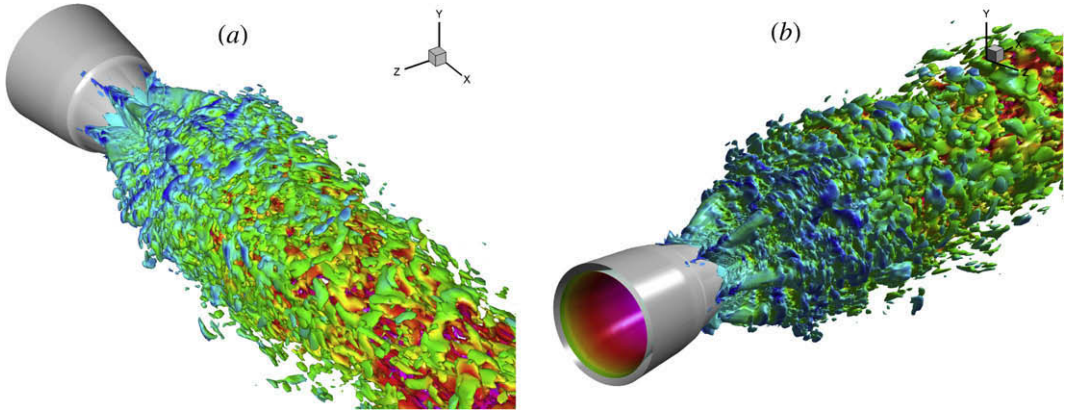

Fig. 9. Vorticity iso-surface (at the value: $|\omega|D/U_j = 2.0$) colored by streamwise velocity magnitude.

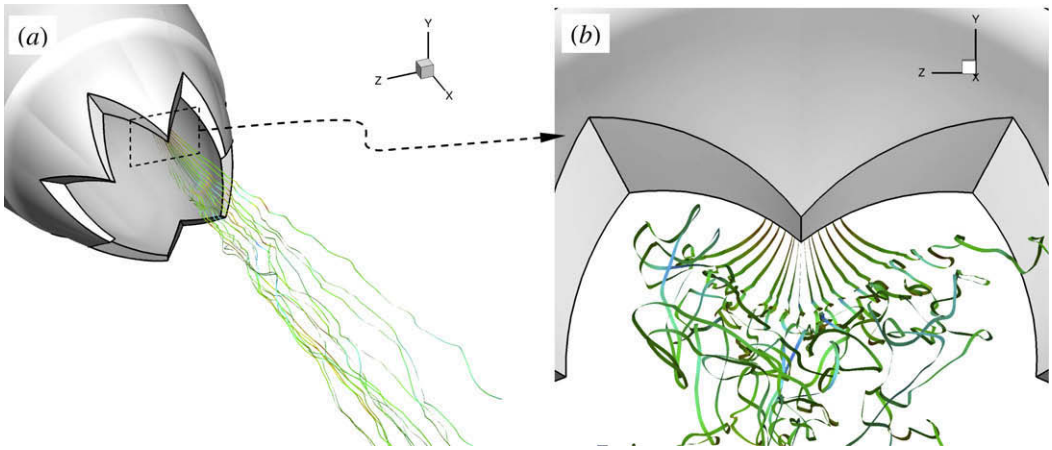

Fig. 10. 'Instantaneous streamlines' near a chevron tip.

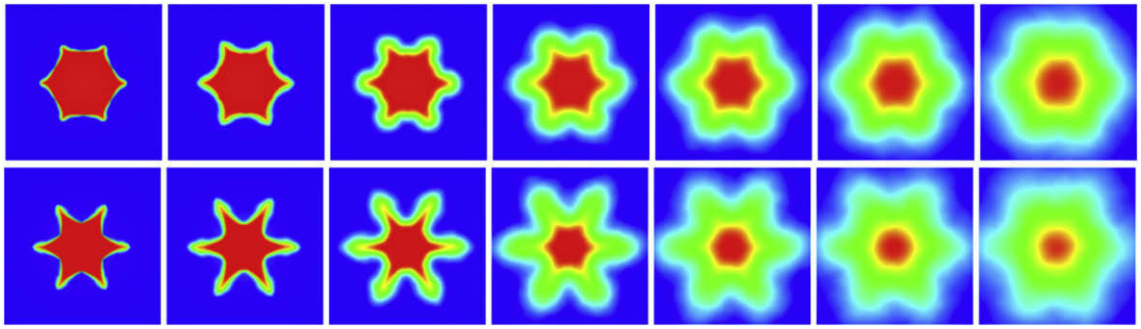

Fig. 11. SMC001 (upper) and SMC006 (lower) mean streamwise velocity contours on z–y planes at $x/D = 0.2$, 0.5, 1, 2, 3, 4 and 5. Red for high values and blue for low.

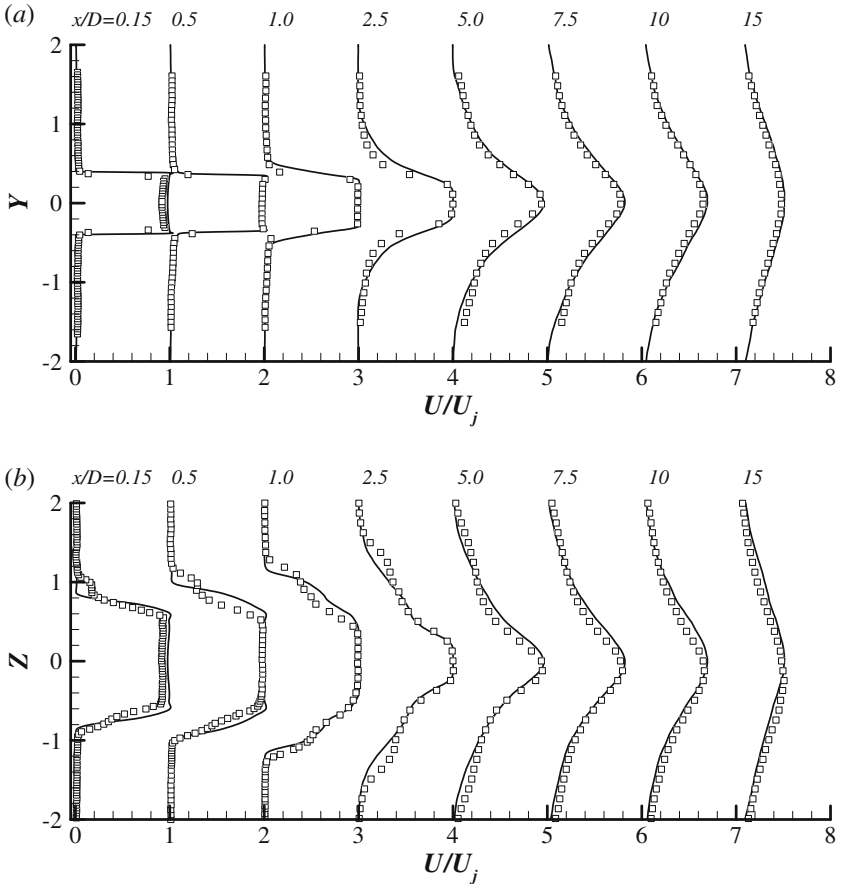

Fig. 12. SMC006 mean streamwise velocity profiles on cut planes (see Fig. 1 for definition) at various x locations. (a) x–y plane ($z = 0$); (b) x–z plane ($y = 0$). —, Prediction; □, Measurements (Bridges and Brown, 2008). Individual profiles are separated by a horizontal offset of 1.0 with the corresponding zero lines located at 0, 1, 2, . . ., 7.

correlation curves at $x = 16D$ and $y = 0$. The two-point velocity correlation in the radial direction at $y = y_0$ is defined as

$$\mathscr{R}_{11}(y_0, \Delta y) = \frac{\overline{u'(y_0,t) \cdot u'(y_0 + \Delta y, t)}}{\overline{u'(y_0,t) \cdot u'(y_0,t)}} \quad (10)$$

where $\Delta y = y - y_0$ is the spatial offset of a point from the base point (x_0, y_0). The coarse grid prediction (dash dot line) is contrasted with the measurements (solid line). Although the computation is based on the very coarse mesh, the correlation curves still show encouraging agreement with the measurements. In Fig. 6, Frame (a) shows the resolved sound propagation. Frame (b) gives the FW–H far-field sound pressure level directivity. In particular, for both grids the predicted far-field sound directivity demonstrates good credibility of the current flow solver and the FW–H integrator. Note the FW–H surface configuration follows the 'S3' surface of Shur et al. (2003) without a full closing disk.

3. Case setup and flow conditions

A key purpose of this study is to highlight the penetration effects of chevrons. Hence, the most severe 18.2° bend SMC006 nozzle is chosen as our primary focus. For comparative purposes the 5° SMC001 is also fully studied. Table 1 gives some basic parameters of the two nozzles. A geometric nozzle representation was shown in Fig. 1. The x–y ($z = 0$) and x–z ($y = 0$) cut planes are identified in Fig. 1. These correspond to slices through a pair of chevron tips and roots and will be referred to later. The origin of the coordinate system is set at the center of the nozzle exit plane.

The isothermal flow condition was defined in Tanna (1977) as SP7, having an acoustic Mach number $Ma_{ac} = U_j/a_\infty = 0.9$ and a temperature ratio $T_j/T_\infty = 0.84$. Table 2 summarizes the actual total and ambient conditions used in the experiments. Based on the jet exit diameter D and jet exit velocity U_j, the Reynolds number is 1.03×10^6.

It is well known that mesh quality can strongly influence LES solutions. Despite its ability to handle complex geometries, an unstructured mesh, such as a tetrahedron dominated one, is often associated with different types of skewness. These can severely damp waves such as acoustic, vortical, or Tollmien–Schlichting. Hence, extra care is needed when using such meshes in an LES context. This is particularly true while performing LES for aero-acoustic predictions. Therefore, hexahedral body-fitted meshes with conformed multi-block structured topologies are used in this study even though the solver itself was designed for generic unstructured meshes.

The fact that chevrons are always azimuthally periodic can substantially reduce mesh generation time, and mesh templates can be used for different nozzles. The mesh for a single chevron can be generated first and copied azimuthally. A singularity treatment is needed for the jet centerline (x axis) thus avoiding clustering polar points or polar lines. Hence, as shown in Fig. 7b and c, a square block is embedded in the middle with four transition blocks between it and the six chevron blocks. Notably, elliptic smoothing

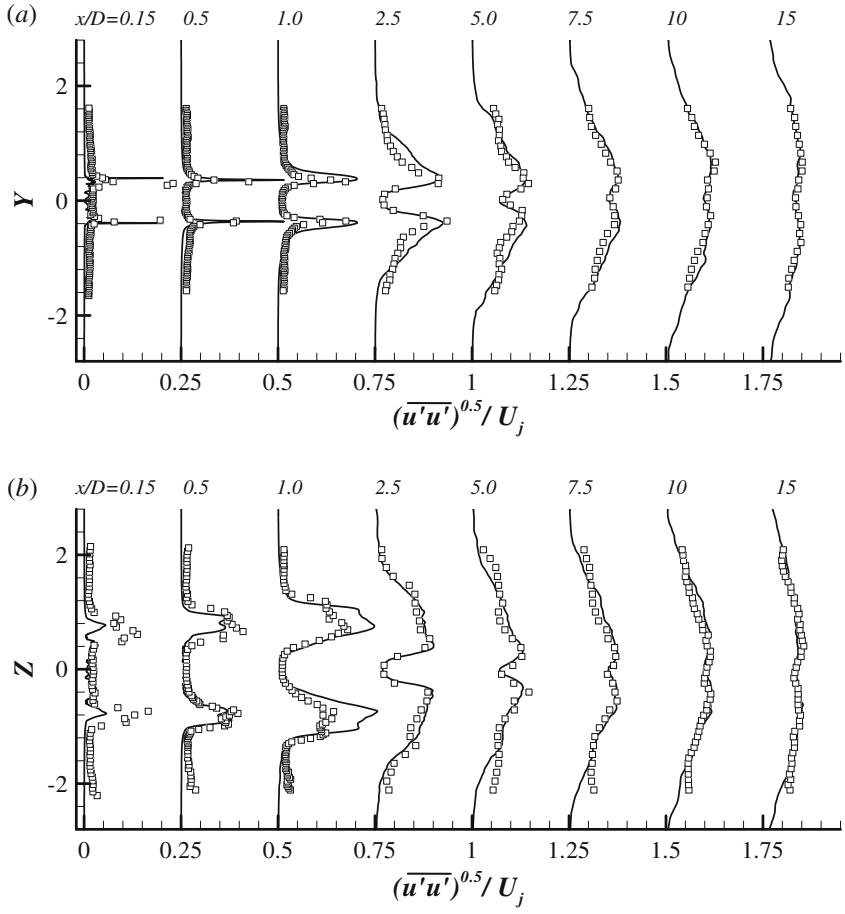

Fig. 13. SMC006 mean profiles of normal Reynolds stress $\overline{u'u'}$ on cut planes at various x locations. Individual profiles are separated by a horizontal offset of 0.25 with the corresponding zero lines located at 0, 0.25, 0.5, . . ., 1.75. (Legends are the same as Fig. 12.)

slightly bent the square block to maintain good orthogonality. There are total 539 streamwise nodes, 167 radial (86 inside the nozzle and 81 outside) and 121 nodes in the circumferential direction. The mesh has a total of 57 blocks and 12.5×10^6 cells. Fig. 7a shows the mesh on the "tip-cut" x–y plane with half of its actual node density. Fig. 7b gives a view of the i-plane folding through the chevron tips and roots. The size of the first off-wall grid cell is controlled such that: $\Delta r^+ \approx 2.5, \Delta x^+ \leqslant 300$, and $\Delta(r\theta)^+ \leqslant 150$ in wall units. In relation to the basic round jet grid density, the total number of grid points is consistent, bearing in mind the $N \propto Re^{0.4}$ requirement (Piomelli, 2008) for hybrid RANS/LES methods. Although there is no meaningful wall boundary in the validation (basic round jet) case, a local grid spacing comparison can still be made based on the shear layer momentum thickness at the end of the potential core. For the basic round jet coarse mesh, $\Delta r/\delta_m \approx 0.17, \Delta x/\delta_m \approx 0.85$, and $\Delta(r\theta)/\delta_m \approx 0.48$. For the chevron case, these values are 0.09, 0.21, and 0.26, which seems reasonable for a modest mesh.

Previous experience suggests that initializing the flow field with a pure RANS solution certainly does not help speed up obtaining the fully matured LES flow field. Hence, solutions are all obtained from quiescent initialization. However, computational time can be saved by maturing the flow on a coarse mesh (2.5×10^6 cells) and interpolating the flow onto the finer mesh. The current physical time step is $\Delta t = 1.0 \times 10^{-7}$ s or in non-dimensional units $\Delta t^* = 5 \times 10^{-4}$ where $t^* = tU_j/D$. Ten inner pseudo time iterations are fixed for each (physical) time step. Around 100,000 time steps are applied to let the flow settle from the initial quiescent state. Another 250,000 time steps are performed for the turbulence statistics and acoustic data accumulation, which is equivalently $t^* = 125$. The parallel scalability of the solver was carefully designed. Load balancing and minimum data exchange among processors is achieved using the graph and mesh partitioning algorithm and software library: METIS of Karypis and Kumar (1995). The solver generally gives a ratio of 90% against the ideal speedup in the current case. On average, every 100,000 time steps on the fine mesh take 100 h on 128 CPU cores (4 cores × 32 nodes). This indicates the potential of pursuing larger scale calculations. However, here it is informative to assess the fidelity of results on more modest meshes. When moving to realistic engine conditions, even highly resolved meshes will effectively be modest. Computations are performed on the Darwin HPC (high performance computing) facility at the University of Cambridge consisting of 2340 processor cores spread over 585 nodes connected via dedicated high speed interconnects and the IBM Deep Computing system (16 CPUs × 22 nodes) at Swansea University.

4. Results and discussion

4.1. Instantaneous flow characteristics

To explore the altered chevron shear layer mixing by the chevrons, the near nozzle instantaneous flow field is examined. Only the results for the much more strongly penetrating SMC006 are presented here. Fig. 8 gives computational snapshots of density gradient magnitude or 'Numerical Schlieren' on both cut planes.

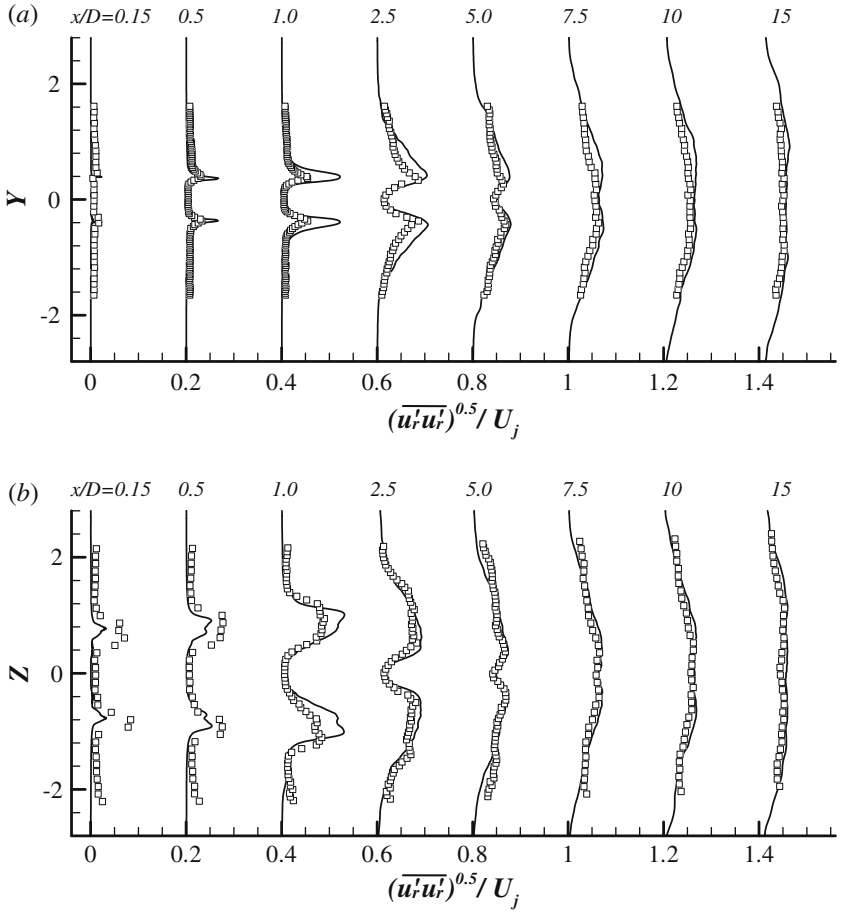

Fig. 14. SMC006 mean profiles of normal Reynolds stress $\overline{u_r' u_r'}$ on cut planes at various x locations. Individual profiles are separated by a horizontal offset of 0.2. (Legends are the same as Fig. 12).

In spite of some density variations within it, the potential core is clearly visible, its length being slightly shorter than 5*D*. Strong density variations are located in the shear layer next to the potential core. The outer edge of the shear layer can also be easily identified. However, there is hardly any fluctuation inside the nozzle, instead, the density gradient is uniform. Comparison of Fig. 8a and b shows that on the root-cut plane the shear layer spreads dramatically while on the tip-cut plane the jet width initially actually decreases. Frame (c) shows the flow is forced out between the chevron roots creating additional shear.

Fig. 9 shows three-dimensional visualizations of the vorticity iso-surface at a non-dimensional value of 2.0. Notably, the vorticity iso-surface emanating from the chevron roots suggests relaminarization of the accelerating flow (relatively smooth iso-surface) before fully retransitioning after about one jet diameter. It is also clear that the jet recovers to a standard round jet after around 10 jet diameters. On the inside nozzle surface the smooth iso-surface is consistent with RANS modeling. However, as already noted the core nozzle interior flow also appears to be laminar (see Fig. 8). This would probably be improved through use of synthetic turbulence at the inflow. Fig. 10 shows 'instantaneous flow streamlines' seeded near a chevron tip. The lines are consistent with vortex roll-up after a short distance from the tip.

4.2. Mean flow and Reynolds stresses

In Fig. 11, mean streamwise velocity contours for SMC001 and SMC006 nozzles are shown for z–y cut planes at $x/D = 0.2$, 0.5, 1, 2, 3, 4 and 5. A typical 'star' shape is identified for both nozzles. As streamwise distance increases, the star shape becomes more smeared and round. As expected, the size of the jet potential core is also seen to decrease with x. Closer to the nozzle exit, the SMC006 nozzle experiences stronger flow penetration the 'star shape' tending to be more clearly defined. The potential core diameter can be seen to decrease slightly faster than for the SMC001. Also, the region between the potential core and the ambient flow seems wider. This indicates a stronger mixing for the SMC006 nozzle, which again is to be expected.

Mean velocity profiles for SMC006 are plotted in Fig. 12. Frame (a) gives profiles on the x–y cut plane through a pair of chevron tips. In Fig. 12b, profiles are on the x–z cut plane through a pair of chevron roots (refer to Fig. 1 for cut plane definition). Streamwise locations are $x/D = 0.15$, 0.5, 1.0, 2.5, 5.0, 7.5, 10 and 15. Individual profiles are separated by a horizontal offset of 1.0. Mean u-velocity profiles on both planes are well captured. For $x/D = 0.5$, 1.0 and 2.5, minor discrepancies can be noticed, essentially related to the predictions having smoother profiles consistent with the less strongly defined flow features observed in the Fig. 12 comparison. For $x/D = 5.0$ the flow is like that of a round jet flow with similar x–y and x–z plane profiles.

Figs. 13 and 14 compare the normal Reynolds stress profiles at the same locations as Fig. 12. Broadly, the agreement with measurements is encouraging especially for the tip planes. However, there are noticeable discrepancies at $x/D = 0.15$ and 1.0. For example, at $x/D = 1.0$, in Fig. 13b the normal Reynolds stress $\overline{u'u'}$ is over-predicted by 25%. Close to the nozzle exit, it seems both normal stresses are underestimated on the root-cut planes, although on

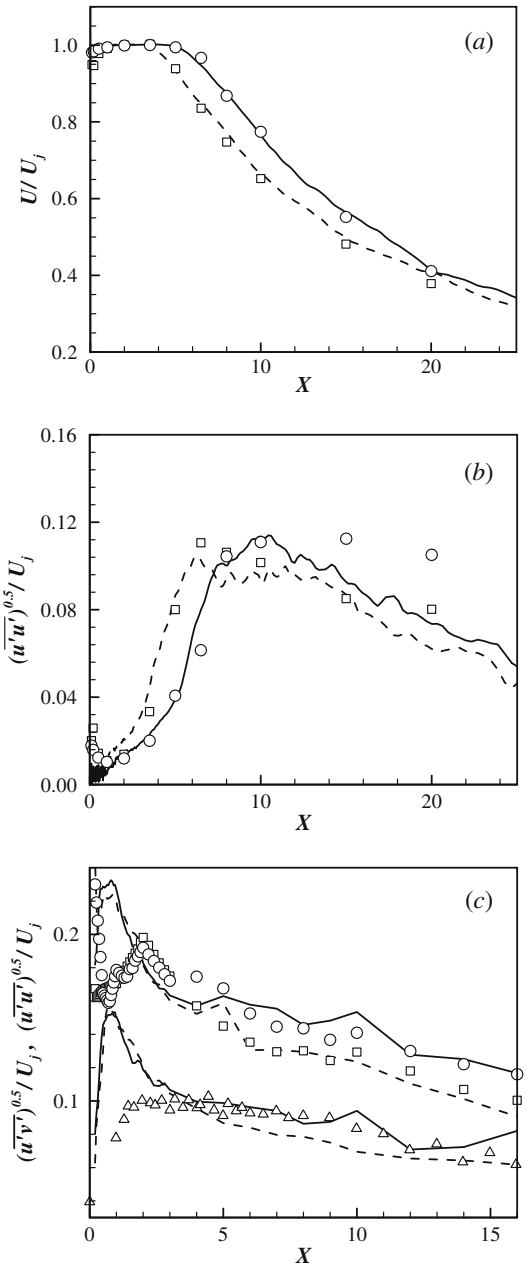

Fig. 15. Comparison of mean velocity and Reynolds stresses for SMC001 and SMC006. (a) Centerline u-velocity; (b) Centerline normal Reynolds stress; (c) Shear layer peak normal and shear Reynolds stress. —, SMC001 prediction; - - -, SMC006 prediction; Measurements (Bridges and Brown, 2008): ○, SMC001; □, SMC006. △, measurements for a round jet (Birch et al., 2006).

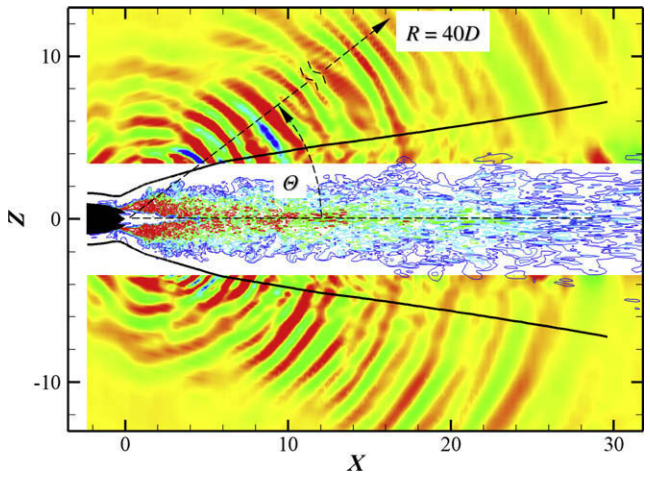

Fig. 16. Representation of the FW–H surface profile (solid line) and the far-field sound observer position, 40*D* away from the jet exit. Background contours: $\partial p/\partial t$ (outer region) and vorticity (inner region).

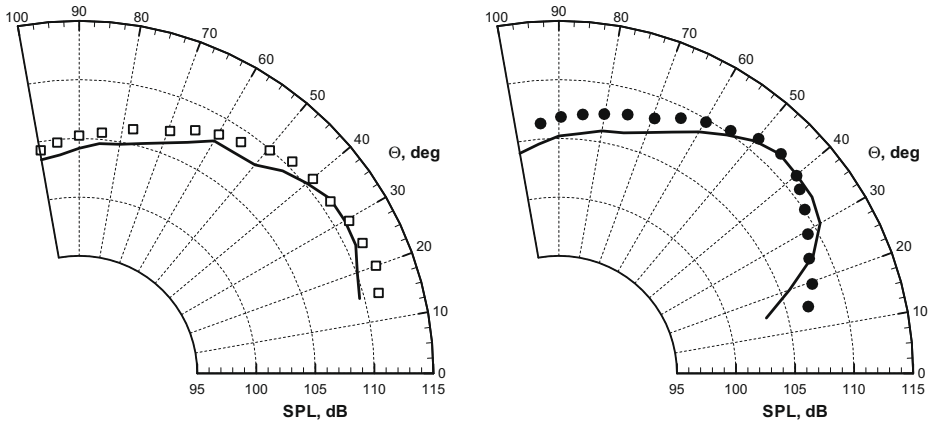

Fig. 17. Far-field sound pressure level directivity at $R = 40D$. —, Predictions. Measurements (Bridges and Brown, 2004): □, SMC001; ●, SMC006.

tip planes they are much better agreed with the measurement. This is primarily due to the current modest mesh resolution in the azimuthal direction, suggesting that 20 nodes per chevron are still not sufficient. The profiles from Frame (a) in both Figs. 13 and 14 can be regarded as the round jet profiles, and the difference between Frames (a) and (b) is the extra Reynolds normal stresses due to the chevron. A round jet characteristic is evident after $x/D = 5.0$ because there is no difference between Frames (a) and (b).

Fig. 15 compares the centerline velocity [Frame (a)], centerline streamwise Reynolds Stress [Frame (b)] and peak shear layer statistics [Frame (c)] for both nozzles with the measurements. For the centerline mean velocity decay in Frame (a), the simulations and measurements are within 2–3% of each other. For the centerline normal Reynolds stress, $\overline{u'u'}$ in Frame (b), the simulation is, on average, within 5% of the measurements. Both Frames (a) and (b) demonstrate the correctly predicted trend that SMC006 has a shorter potential core than SMC001, which is observed previously in Fig. 12. There is a small amount of oscillation in Frame (b) at $0 < x < 1$. Links between this and the change of the ε value cannot be ruled out. However no numerical instability has been observed near this region. Also, the level of the oscillation is lower than the experimental value. In Frame (c), $\overline{u'u'}$ and $\overline{u'u'_r}$ are plotted against axial distance in the shear layer. As the shear stress measurements for chevron nozzles are not available, the measured shear stress for a round jet from Birch et al. (2006) is taken as a reference. It is unclear what causes disagreement in peak normal stress near the nozzle exit around $x/D = 1.0$. Experiment wise, this is close to the upstream boundary of the PIV area hence the accuracy of the measurement might be compromised. Numerically this is also the transient region from RANS to ILES, and the level of mixing in the coming flow may not be sufficient since there is no turbulent fluctuation has been imposed at the upstream boundary. Nevertheless, further away from this zone the primary shear stress and normal stress values seem more accurate.

4.3. Far-field sound

As with Fig. 6b, the time derivative of static pressure is used to visualize the sound radiation. Fig. 16 presents the $\partial p/\partial t$ contours on the x–y (tip) cut plane. The central region of high $\partial p/\partial t$, usually indicating pseudo sound, is replaced by vorticity contours.

In Fig. 16, the FW–H surface is also identified. The current FW–H surface is tuned and has been validated for the round jet discussed in Section 2.6. Whether the left and right end closing discs should be included has been broadly discussed by Shur et al. (2005) and Freund et al. (1996). It is not surprising that better far-field sound predictions might be gained by tuning the closing discs. However, it is not the interest of this paper to study such influences, hence open surfaces are used. As shown in Fig. 16, the open surface is $30D$ in length, and has diameters of $3D$ and $15D$ on its left and right hand end. The FW–H integral from the far-field sound post-processor calculates the overall sound pressure level (dB) at $40D$ from the nozzle exit center at polar angles of Θ.

Fig. 17 shows encouraging agreements between the predicted far-field sound pressure level (SPL) and the measurements for SMC001 and SMC006, where SPL is given by:

$$\mathrm{SPL} = 20\log_{10}\left(\frac{p'_{rms}}{2\times 10^{-5}\ \mathrm{Pa}}\right) \tag{11}$$

The root-mean-square pressure fluctuation p'_{rms} is obtained from the FW–H integrated far-field pressure perturbation p' in the time domain. To further examine the effects of SMC006's stronger penetration, Fig. 18 compares the difference of sound pressure level: $\Delta\mathrm{SPL} = \mathrm{SPL}_{\mathrm{SMC006}} - \mathrm{SPL}_{\mathrm{SMC001}}$ obtained from the current predictions and the measurements. Except for the overshoot near $\Theta = 50°$ (1.3 dB discrepancy), the predictions agree with the measurements to 1 dB. More importantly, this numerical study confirms the phenomenon observed in the experiments. For example, at lower (or downstream) polar angles chevrons tend to reduce the noise dramatically. However, at higher angles they increase the noise slightly.

Fig. 19a contrasts instantaneous x-vorticity contours for the SMC001 and SMC006 nozzles. To help approximately understand the effects of chevron penetration on far-field sound, the contours of the nominal sound source on the z–y plane at $x/D = 1.5$ are

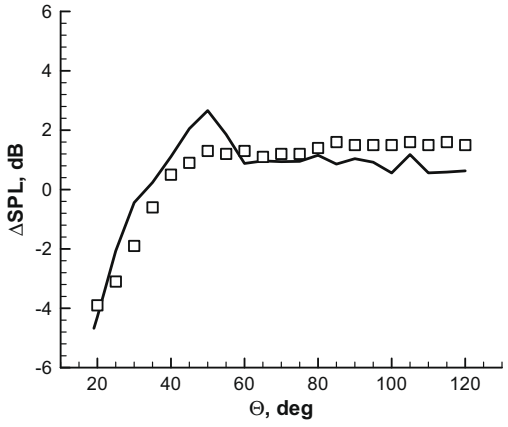

Fig. 18. Far-field sound pressure level increase of SMC006 compared with SMC001. —, Prediction. □, Measurements (Bridges and Brown, 2004).

plotted in Fig. 19b. By recasting the flow equations into a wave equation, the acoustic source is then given by:

$$S = a_\infty^2 \left[\frac{\partial^2(\bar{\rho}\tilde{u}_i\tilde{u}_j)}{\partial x_i \partial x_j} - \frac{\partial^2 \tilde{\tau}_{ij}}{\partial x_i \partial x_j} \right] + \frac{\partial^2}{\partial t^2}(\bar{p} - a_\infty^2 \bar{\rho}) \tag{12}$$

Fig. 19 shows that the distributions of both the vorticity and 'nominal' acoustic source differ between the two nozzles. For SMC006 the stronger mixing indicated by the x-vorticity is consistent with the fact the source is more expanded in the radial direction. The patterns of stream-wise vorticity are similar to the acoustic source.

Figs. 20 and 21 show the power spectral density (PSD) of the far-field sound at two different polar angles: $\Theta = 30°$ and 90°, for SMC001 and SMC006 respectively. As can be seen, the simulations also capture the broadband spectra at correct dominant frequencies up to $St = 2.0$. The predicted high-frequency spectra decay too fast. Also, at low frequencies, although the right level has been predicted, even longer time histories would be beneficial. Fig. 22 compares both the predictions and measurements for the SMC001 and SMC006 spectra at 90°. One of the experimentally observed features is that stronger chevron penetration reduces the low-frequency noise while increasing high-frequency. The predic-

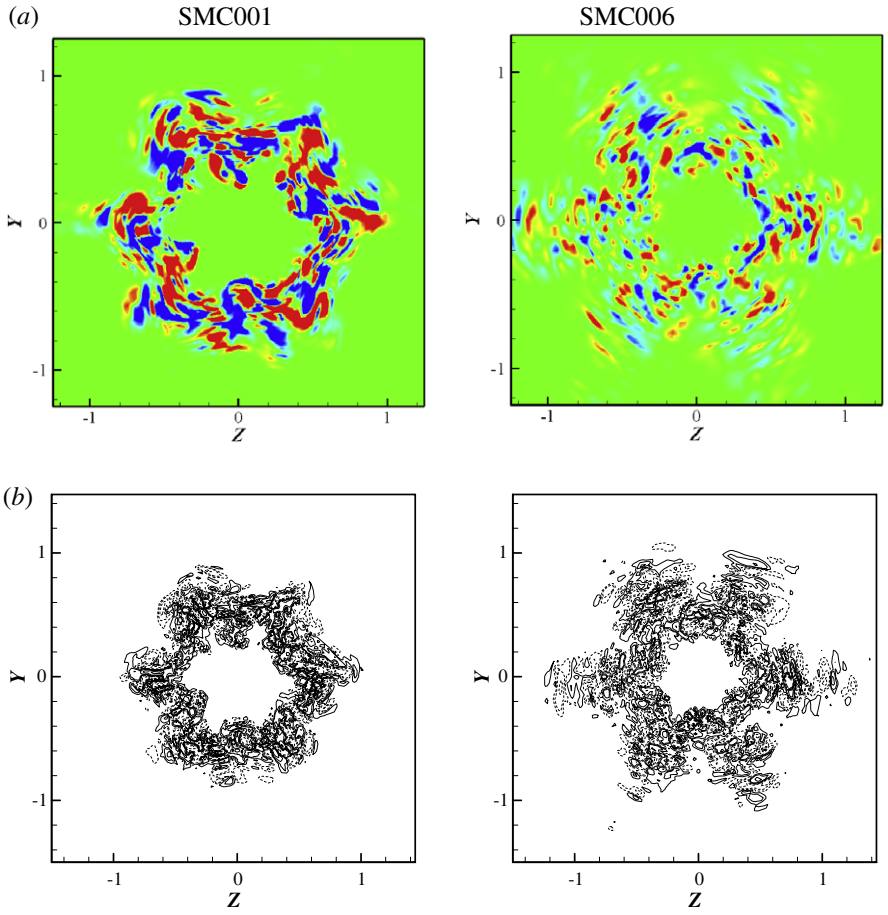

Fig. 19. Instantaneous contours of (a) stream-wise vorticity: $-3.5 < \omega_x(D/Uj) < 3.5$; and ($b$) 'nominal' acoustic source S on z–y plane at $x/D = 1.5$: —, positive levels; - - - negative levels.

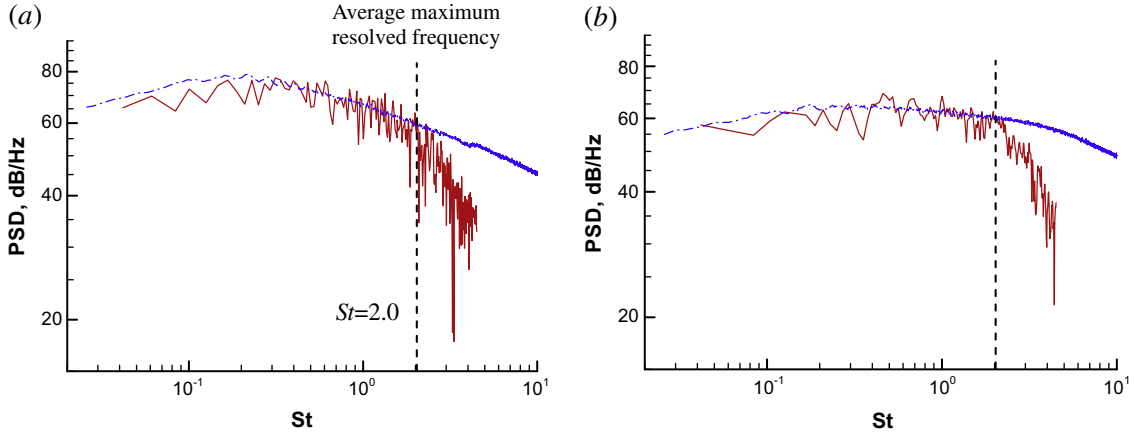

Fig. 20. Far-field sound PSD for SMC001 at $R = 40D$. (a) $\Theta = 30°$. (b) $\Theta = 90°$.

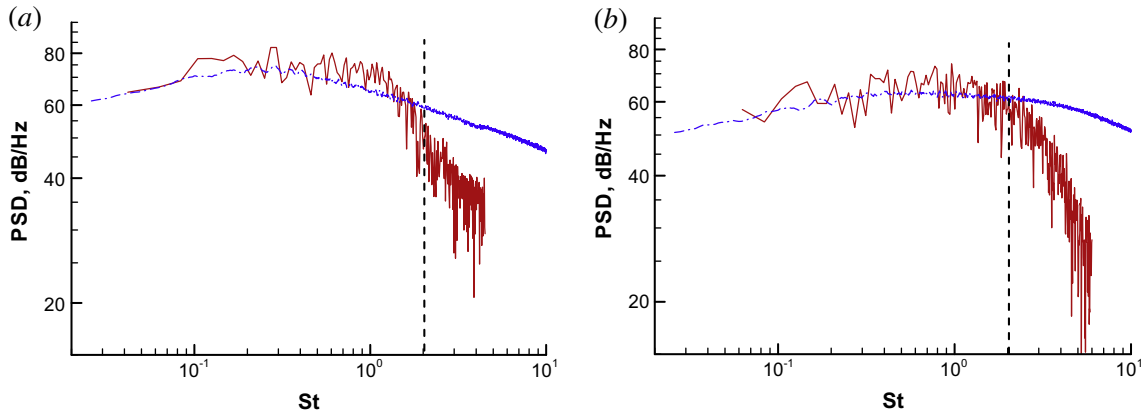

Fig. 21. Far-field sound PSD for SMC006 at $R = 40D$. (a) $\Theta = 30°$. (b) $\Theta = 90°$.

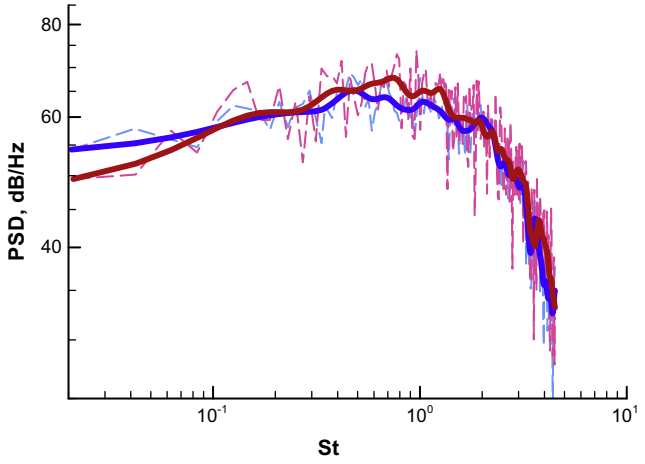

Fig. 22. Comparison of the predicted PSD for SMC001 (blue) and SMC006 (red) at 90°. – – –, raw; —, filtered. (For interpretation of the references to colour in this figure legend, the reader is referred to the web version of this article.)

tions capture this trend but for the current modest meshes quantitative differences are evident. For example, Fig. 22 shows that SMC006 starts to generate more noise than SMC001 at $0.15 < St < 0.45$. For the measurements the range is about $0.45 < St < 1.2$.

Following Shur et al. (2003), to give an indication of grid resolution effects when capturing high frequencies an estimate of the resolved Strouhal number can be made. Based on grid spacing Δ, this estimate is given as: $St_{max} < a_\infty/(4\Delta)$. Hence, the variation of Δ on the FW–H surface, from $0.006D$ to $0.028D$ in the current case, gives the range of the maximum resolvable frequencies, as $St_{max} \approx 0.52$–3.46. The latter value is ambitious, based on the local maximum grid spacing in the 'finest' region. The majority of the grid spacing suggests $St_{max} \approx 0.52$–2.0. This estimate shows that the grid is still insufficient for an accurate resolution of the frequency components higher than $St = 2.0$. But for the more significant frequency range, as shown in Figs. 17 and 18, with the current grid resolution, an acceptable accuracy for the integral sound intensity can still be achieved.

5. Conclusions

Hybrid large-eddy type simulations and noise predictions have been carried out for two chevron nozzles. A robust flow solver and a FW–H integrator are used to. The validation of these elements for a basic round jet is given. Near wall RANS modeling is coupled to ILES through a Hamilton–Jacobi equation. FW–H integrals have been computed to obtain the far-field sound directivity and power spectral density. The hybrid RANS–ILES has demonstrated encouraging capabilities on the modest 12.5 million-cell mesh. Favorable agreement with the mean velocity and Reynolds stress measurements has been broadly gained. The credibility of the current methodology is also supported by the far-field sound predictions such as the SPL directivity and PSD. As a result of the grid resolution limit, higher frequency components of the broadband noise have not been captured, but for the dominant frequency range $St = 0.02$–2.0 the predictions are encouraging.

The numerical simulation confirms the experiment with respect to the influence of chevron penetration. With a bend angle of 18.2°, the potential core is shorter, downstream Reynolds stresses lower, but the sound source distribution wider in the side line direction. The characteristics of far-field sound for the 18.2° bend are therefore to the bend angle of 5°. Namely, the more server bend has louder side line but quieter downstream noise. It also increases the high-frequency sound intensity but decreases the low-frequency. This consistency of the current numerical study with measurements is encouraging and suggesting a reliable numerical framework has been developed.

Acknowledgements

This work was financially supported by UK Engineering and Physical Sciences Research Council (EPSRC) under grant number GR/T06629/01. Tucker would like to acknowledge funding under the Royal Society Industry Fellowship Scheme. The authors specially appreciate the communications with Drs James Bridges, Cliff Brown and Nick Georgiadis from NASA Glenn Research Center and the supply of experimental data. The Darwin HPC facility at the University of Cambridge and the IBM Deep Computing system at Swansea University are gratefully acknowledged. The authors also thank the reviewers for their valuable comments and suggestions.

References

Birch, S.F., Lyubimov, D.A., Maslov, V.P., Secundov, A.N., 2006. Noise prediction for chevron nozzle flows. In: 12th AIAA/CEAS Aeroacoustics Conference, May 2006, AIAA Paper 2006-2600.

Bodony, D., Lele, S., 2008. Current status of jet noise predictions using large-eddy simulation. AIAA Journal 46 (2), 2008.

Bogey, C., Bailly, C., 2005. Effects of inflow conditions and forcing on subsonic jet flows and noise. AIAA Journal 43 (5), 2005.

Bridges, J., Wernet, M., 2003. Measurements of the aeroacoustic sound sources in hot jets. In: 9th AIAA/CEAS Aeroacoustics Conference, South Carolina, 12–14th May 2003, Paper No. AIAA-2003-3130.

Bridges, J., Brown, C., 2004. Parametric testing of chevrons on single flow hot jets. In: 10th AIAA/CEAS Aeroacoustics Conference, Manchester, UK, May 2004, AIAA Paper 2004-2824.

Bridges, J., Brown, C., 2008. Aerodynamic and aeroacoustic measurements of the SMC series chevron jets. Private Communication.

Brown, C., Bridges, J., 2006. Small hot jet acoustic rig validation, NASA/TM 2006-214234.

Bui, T., 1999. A Parallel, Finite-volume algorithm for large-eddy simulation of turbulent flows, NASA/TM-1999-206570.

Chow, FK., Moin, P., 2003. A further study of numerical errors in large eddy simulations. Journal of Computational Physics 184, 366–380.

Chung, Y.M., Tucker, P.G., 2003. Accuracy of higher-order finite difference schemes on nonuniform grids. AIAA Journal 41 (8), 1609–1611.

Colonius, T., 2004. Modeling artificial boundary conditions for compressible flow. Annual Review of Fluid Mechanics 36, 315–345.

Engblom, W.A., Khavaran, A., Bridges, J., 2004. Numerical prediction of chevron nozzle noise reduction using wind-mgbk methodology. In: 10th AIAA/CEAS Aeroacoustics Conference 2004, AIAA Paper 2004-2979.

Ffowcs Williams, J.E., Hawkings, D.L., 1969. Sound generation by turbulence and surfaces in arbitrary motion. Philosophical Transactions of Royal Society of London 264A, 321–342.

Freund, J.B., Lele, S.K., Moin, P., 1996. Calculation of the radiated sound field using an open Kirchhoff surface. AIAA Journal 34 (5), 909–916.

Ghosal, S., 2002. An analysis of numerical errors in large eddy simulations of turbulence. Journal of Computational Physics 125, 187–206.

Grinstein, F.F., Fureby, C., 2002. Recent progress on miles for high Reynolds number flows. ASME Journal of Fluids Engineering 124 (December), 848–861.

Karypis G., Kumar, V., 1995. A fast and high quality multilevel scheme for partitioning irregular graphs. In: International Conference on Parallel Processing, pp. 113–122.

Kenzakowski, D.C., Shipman, J., Dash, S.M., 2000. Study of three-stream laboratory jets with passive mixing enhancements for noise reduction, AIAA Paper 2000-0129.

Liu, Y., Tucker, P.G., Kerr, R.M., 2008. Linear and non-linear large-eddy simulations of a plane jet. Computers and Fluids 37, 439–449.

Lush, P.A., 1971. Measurements of subsonic jet noise and comparison with theory. Journal of Fluid Mechanics 46, 477–500.

Mary, I., Sagaut, P., 2002. Large eddy simulation of flow around an airfoil near stall. AIAA Journal 40 (6), 1139–1145.

Massey, S.J., Elmiligui, A.A., Hunter, C.A., Thomas, R.H., Pao, S.P., Mengle, V.G., 2006. Computational analysis of a chevron nozzle uniquely tailored for propulsion airframe aeroacoustics. In: 12th AIAA/CEAS Aeroacoustics Conference, May 2006, AIAA Paper 2006-2436.

Piomelli, U., 2008. Wall-layer models for large-eddy simulations. Progress in Aerospace Sciences 44, 437–446.

Roe, P.L., 1981. Approximate Riemann solvers, parameter vectors and difference schemes. Journal of Computational Physics 43, 357–372.

Rudy, D.H., Strikwerda, J.C., 1980. Boundary conditions for subsonic compressible Navier–Stokes calculations. Computers and Fluids 9, 327–338.

Saiyed, N., 1997. Separate flow nozzle test status meeting, NASA/TM 2000-210524.

Saiyed, N., Mikkelsen K.L., Bridges, J., 2000. Acoustics and thrust of separate-flow exhaust nozzles with mixing devices for high-bypass-ratio engines, NASA/TM 2000-209948.

Sethian, J.A., 1999. Level set Methods and Fast Marching Methods. Cambridge University Press.

Shur, M.L., Spalart, P.R., Strelets, M.Kh., Travin, A.K., 2003. Towards the prediction of noise from jet engines. International Journal of Heat and Fluid Flow 24, 551–561.

Shur, M.L., Spalart, P.R., Strelets, M.K., 2005. Noise prediction for increasingly complex jets. Part ii: Applications. International Journal of Aeroacoustics 4 (34), 247–266.

Shur, M. L., Spalart, P.R., Strelets, M.K., Garbaruk, A.V., 2006. Further steps in les-based noise prediction for complex jets. 44th AIAA Aerospace Sciences Meeting and Exhibit, 9–12 January 2006, AIAA Paper 2006-485.

Spalart, P.R., Allmaras, S.R., 1992. A one-equation turbulence model for aerodynamic flows. AIAA Paper 92-0439, January 1992.

Tanna, H.K., 1977. An experimental study of jet noise: part I turbulent mixing noise. Journal of sound and Vibration 50 (3), 405–428.

Thomas, R.H., Kinzie, K.W., Pao, S.P., 2001. Computational analysis of a pylon–chevron core nozzle interaction, AIAA Paper 2001-2185.

Thompson, K.W., 1987. Time-dependent boundary conditions for hyperbolic systems. Journal of Computational Physics 68, 1–24.

Tucker, P.G., 2002. Differential equation based distance computations for DES and RANS. Journal of Computational Physics 190 (1), 229–248.

Tucker, P.G., 2004. Novel miles computations for jet flows and noise. International Journal of Heat and Fluid Flow 25 (4), 625–635.

Tucker, P.G., 2006. Turbulence modelling for problem aerospace flows. International Journal for Numerical Methods in Fluids 51 (3), 261–283.

Tucker, P., Coupland, J., Eastwood, S., Xia, H., Liu, Y., Loveday, R., Hassan, O. 2006. Contrasting code performances for computational aeroacoustics of jets. In: 12th AIAA Aeroacoustics Conference, Cambridge, Massachusetts, 8–10 May 2006 Paper No 2006-2672.

Uzun, A., Hussaini, M.Y., 2007. Noise generation in the near-nozzle region of a chevron nozzle jet flow. In: 13th AIAA/CEAS Aeroacoustics Conference 2007, AIAA Paper 2007-3596.

van Leer, B., 1979. Towards the ultimate conservative difference scheme, v. a second order sequel to Godunov's method. Journal of Computational Physics 32, 101–136.

Wu, X., Jacobs, R., Durbin, P., 1999. Simulation of boundary layer transition induced by periodically passing wake. Journal of Fluid Mechanics 398, 109–153.

Xia, H., 2005. Dynamic grid detach-eddy simulation for synthetic jet flows. PhD thesis, The University of Sheffield.

Xia, H., Tucker, P.G., Eastwood, S.J., 2008. Towards jet flow LES of conceptual nozzles for acoustic predictions. 46th AIAA Aerospace Sciences Meeting and Exhibit, 7–10 January 2008, AIAA Paper 2008-10.